

On the parametric instability of multilayered conical shells using the FOSDT

John Lair ^{1a}, David Hui ^{1b}, Abdullah H. Sofiyevev ^{*2}, Viktor Gribniak ^{3c} and Ferruh Turan ^{4d}

¹ Department of Mechanical Engineering, University of New Orleans, New Orleans, Louisiana, USA

² Department of Civil Engineering, Faculty of Engineering, Suleyman Demirel University, Isparta, Turkey

³ Laboratory of Innovative Building Structures, Vilnius Gediminas Technical University, Vilnius, Lithuania

⁴ Department of Civil Engineering, Faculty of Engineering, Ondokuz Mayıs University, Samsun, Turkey

(Received October 2, 2018, Revised March 17, 2019, Accepted March 20, 2019)

Abstract. This paper investigates the parametric instability (PI) of multilayered composite conical shells (MLCCSs) under axial load periodically varying the time, using the first order shear deformation theory (FOSDT). The basic equations for the MLCCSs are derived and then the Galerkin method is used to obtain the ordinary differential equation of the motion. The equation of motion converted to the Mathieu-Hill type differential equation, in which the DI is examined employing the Bolotin's method. The expressions for left and right limits of dimensionless parametric instability regions (PIRs) of MLCCSs based on the FOSDT are obtained. Finally, the influence of various parameters; lay-up, shear deformations (SDs), aspect ratio, as well as loading factors on the borders of the PIRs are examined.

Keywords: composite structures; dynamic analysis; instability; vibration; axial load

1. Introduction

In modern designs of the most diverse type and purpose, multilayered composite cylindrical and conical shells are very widespread and therefore of interest. Detailed studies of the shells used in engineering lead to the conclusion that they are often anisotropic and in many cases are anisotropic and laminated. In the open literature there are fundamental studies devoted to the theory of anisotropic layered shells (Ambartsumian 1961, Hui 1985, Reddy 2004). These studies shed light on many fundamental problems of the theory of anisotropic layered shells. The great interest of researchers in improved theories of laminated shells is the fact that the classical shell theory (CST) is incomplete, and the results obtained in many cases are unacceptable for problems of moderately thick laminated anisotropic shells.

In some applications of the multilayered composite shells, they can be subjected to the axial load periodically varying with the time. Therefore, the study of the dynamic response of layered shells under axial dynamic loading is very important for ensuring the safety and reliability of laminated shells. The parametric instability may occur when there is a correlation between the natural frequencies of the shell and the axial force frequency. The range of values of the parameters that cause unstable motion is called the parametric instability regions (PIRs).

The first attempts to solve the dynamic instability (DI) problem of laminated anisotropic shells have been started for half a century (Goroshko and Emel'yanenko 1975). Argento and Scott (1993) used perturbation technique together with Donnell shell theory to determine the DIRs of composite circular cylindrical shells. Liao and Cheng (1994) used a three-dimensional degenerate shell element model to study the DI under in-plane vibrational forces of stiffened laminated composite shells and employed the perturbation technique with multiscale method to determine DIRs. Ganapathi and Balamurugan (1998) used the finite element method to investigate the parametric resonance of laminated anisotropic composite shell structures subjected to periodic axial/radial loading. Ng and Lam (1999) conducted a comprehensive study of various aspects of the PI of multi-layered shells using different shell theories. Wu and Chiu (2002) investigated the DI of laminated composite conical shells subjected to static and periodic thermal loads, using the perturbation method, the differential quadrature method and the Bolotin method. Kumar *et al.* (2005) presented the PI characteristics of laminated composite double curved panels subjected to partially distributed follower edge loading. Pradyumna and Bandyopadhyay (2011) studied the DI behavior for two-layered composite shells using C0 finite elements and the higher order shear deformations theory. Fazilati and Ovesy (2010), (Ovesy and Fazilati 2014) developed a semi-analytical and also a Bézier-spline finite strip formulation based on classical plates and shells theories to calculate the PIRs of flat and curved composite structures under uniform and non-uniform in-plane loads. Qinkai and Fulei (2013) studied PI of the rotating truncated conical shells under periodic axial loads. Dey and Ramachandra (2014) analyzed static and DI of composite cylindrical shell panels subjected to partial edge loading. Panda *et al.* (2015) devoted to the analysis of

*Corresponding author, Ph.D.,
E-mail: abdullahavey@sdu.edu.tr

^a Ph.D.

^b Ph.D.

^c Ph.D.

^d Ph.D. Student

the finite elements of the characteristics of the PI of layered bi-directional glass/epoxy composite panels subjected to a hygrothermal field with a harmonic planar load based on the first order shear deformation theory. Awrejcewicz *et al.* (2016) proposed a method for studying DI and nonlinear parametric vibrations of symmetrically laminated plates of complex shape and having different cutouts using the FOSDT and the classical plate theory (CPT). Darabi and Ganesan (2016, 2017) examined DI analysis of laminated cylindrical shells and internally-thickness-tapered laminated plates subjected to harmonic in-plane loading parametric excitations. Biswal *et al.* (2017) presented PI of woven fiber laminated glass/epoxy composite shallow shells in hygrothermal environment based on the FOSDT using the finite element method. Avramov *et al.* (2017) analyzed the DI of a shallow shell in a subsonic air flow using the finite degree of the dynamic freedom system. Pour *et al.* (2017) examined dynamic stability of embedded viscoelastic piezoelectric separators using different cylindrical shell theories. Sofiyev and Kuruoglu (2018) presented the determination of the excitation frequencies of laminated orthotropic non-homogeneous conical shells, based on the classical shell theory (CST).

In recent years, several studies have been carried out using different shell theories concerning the buckling and vibration of multilayered shells (Alankaya and Oktem 2016, Ferreira *et al.* 2011, Shariyat 2011, Biswal *et al.* 2016, Ferreira *et al.* 2016, Khayat *et al.* 2016, Laoufi 2016, Tornabene *et al.* 2016, 2017, Brischetto *et al.* 2017, Caliri Jr. *et al.* 2017, Sofiyev *et al.* 2017, Sofiyev and Kuruoglu 2018, Hu and Chen 2018, Ma *et al.* 2018).

A review of the literature shows that a limited number of studies on the PI of the multilayered conical shells based on the shear deformation theories (SDTs) and insufficiently studied the topic under consideration. In this study, the authors partially fill this gap.

2. Problem formulation

The truncated conical shell under consideration (see Figs. 1(a) and (b)) is assumed to be laminated and composed of N layers of equal thickness and each layer is made of orthotropic materials. The truncated conical shell is of the length L , the semi-vertex angle α , the small and large radii R_1 and R_2 , respectively and the total thickness h . We also assume that after deformation the layers remain elastic and do not slip during deformation. The radial, circumferential and meridional co-ordinates are denoted by, z , θ and r , and the corresponding displacements on the shell reference surface are in turn denoted by w , v and u as shown in Fig. 1.

The elasticity moduli and density of orthotropic materials in the k^{th} layer are $E_{11}^{(k)}$, $E_{22}^{(k)}$, $G_{12}^{(k)}$, $G_{13}^{(k)}$, $G_{23}^{(k)}$ and $\rho^{(k)}$, $\nu_{12}^{(k)}$ and $\nu_{21}^{(k)}$ are the Poisson's ratios in the k^{th} layer and satisfied $\frac{E_{11}^{(k)}}{E_{22}^{(k)}} = \frac{\nu_{12}^{(k)}}{\nu_{21}^{(k)}}$. The principal directions of Young's moduli coincide with the coordinate axes r and θ . Let the MLCCS be subjected to a periodic axial load as a function of time

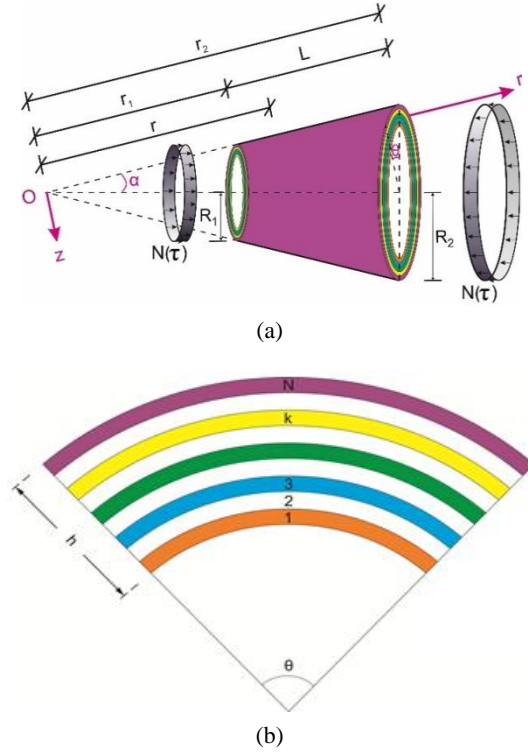


Fig. 1 (a) MLCCS subjected to a periodic axial load as a function of time; and (b) lay-up

$$\begin{aligned} n_{11}^0 &= -N(\tau) = -N_{ax} - N_{axd} \cos(\varpi\tau), \\ n_{22}^0 &= n_{12}^0 = 0 \end{aligned} \quad (1)$$

where n_{11}^0 , n_{22}^0 and n_{12}^0 are the membrane forces, N_{ax} and N_{axd} are the static axial load and the amplitude of the time dependent periodic axial load, and ϖ denotes the excitation frequency of the axial load and τ is a time variable (Bolotin 1964, Sofiyev and Kuruoglu 2018).

2.1 Basic equations

In this study is used the FOSDT which was developed by Ambartsumian (1961). The advantages of this theory over the other FOSDT are that the number of independent unknowns is four and no shear correction factors are required. Let ψ be the stress function for the force resultants (n_{11} , n_{22} , n_{12})

$$\begin{pmatrix} n_{11} \\ n_{22} \\ n_{12} \end{pmatrix} = \begin{pmatrix} \frac{1}{r^2} \frac{\partial^2 \psi}{\partial \varphi^2} + \frac{1}{r} \frac{\partial \psi}{\partial r} \\ \frac{\partial^2 \psi}{\partial r^2} \\ -\frac{1}{r} \frac{\partial^2 \psi}{\partial r \partial \varphi} + \frac{1}{r^2} \frac{\partial \psi}{\partial \varphi} \end{pmatrix}, \quad \varphi = \theta \sin \alpha \quad (2)$$

The governing Donnell-type parametric instability and compatibility equations for the MLCCSs within the FOSDT can be expressed in terms of a stress function ψ , two rotations ϕ_1 and ϕ_2 , and transverse displacement w (Sofiyev *et al.* 2017, Sofiyev and Kuruoglu 2018). They are

$$\begin{aligned}
& -u_{13} \frac{\partial^4 w}{\partial r^4} - \frac{u_{14} + u_{32}}{r^2} \frac{\partial^4 w}{\partial r^2 \partial \varphi^2} \\
& + \frac{3u_{14} + 3u_{32} + u_{24}}{r^3} \frac{\partial^3 w}{\partial r \partial \varphi^2} \\
& - \frac{u_{13} + u_{14} - u_{23}}{r} \frac{\partial^3 w}{\partial r^3} \\
& + \frac{u_{13} + u_{14} - u_{23} + u_{24}}{r^2} \frac{\partial^2 w}{\partial r^2} \\
& - \frac{3(u_{14} + u_{24} + u_{32})}{r^4} \frac{\partial^2 w}{\partial \varphi^2} - \frac{2u_{24}}{r^3} \frac{\partial w}{\partial r} \\
& + u_{15} \frac{\partial^3 \phi_1}{\partial r^3} + \frac{u_{15} - u_{25}}{r} \frac{\partial^3 \phi_1}{\partial r^2} + \frac{u_{35}}{r^2} \frac{\partial^3 \phi_1}{\partial r \partial \varphi^2} \\
& - u_3 \frac{\partial \phi_1}{\partial r} - \frac{u_{15} - u_{25}}{r^2} \frac{\partial \phi_1}{\partial r} - \frac{u_{35}}{r^3} \frac{\partial^2 \phi_1}{\partial \varphi^2} \\
& + \frac{u_{38} + u_{18}}{r} \frac{\partial^3 \phi_2}{\partial r^2 \partial \varphi} - \frac{u_{28} + u_{18} + u_{38}}{r^2} \frac{\partial^2 \phi_2}{\partial r \partial \varphi} \\
& + \frac{2u_{28}}{r^3} \frac{\partial \phi_2}{\partial \varphi} = 0
\end{aligned} \tag{3}$$

$$\begin{aligned}
& - \frac{u_{32} + u_{23}}{r} \frac{\partial^4 w}{\partial r^2 \partial \varphi^2} - \frac{u_{24}}{r^2} \frac{\partial^3 w}{\partial r \partial \varphi^2} \\
& - \frac{u_{24}}{r^3} \frac{\partial^4 w}{\partial \varphi^2} + \frac{u_{25} + u_{35}}{r} \frac{\partial^3 \phi_1}{\partial r \partial \varphi^2} \\
& + \frac{u_{35}}{r^2} \frac{\partial^2 \phi_1}{\partial \varphi^2} + u_{38} \frac{\partial^3 \phi_2}{\partial r^2 \partial \varphi} + \frac{2u_{38}}{r} \frac{\partial^2 \phi_2}{\partial r \partial \varphi} \\
& + \frac{u_{28}}{r^2} \frac{\partial^3 \phi_2}{\partial \varphi^3} - u_4 \frac{\partial \phi_2}{\partial \varphi^2} = 0
\end{aligned} \tag{4}$$

$$\begin{aligned}
& \frac{v_{11} h}{r^4} \frac{\partial^4 \psi}{\partial \varphi^4} + \frac{(2v_{31} + v_{21} + v_{12}) h}{r^2} \frac{\partial^4 \psi}{\partial r^2 \partial \varphi^2} \\
& - \frac{2(v_{31} + v_{21}) h}{r^3} \frac{\partial^3 \psi}{\partial r \partial \varphi^2} + \frac{2(v_{31} + v_{21} + v_{11}) h}{r^4} \frac{\partial^2 \psi}{\partial \varphi^2} \\
& + \frac{v_{11} h}{r^3} \frac{\partial \psi}{\partial r} - \frac{y_{11} h}{r^2} \frac{\partial^2 \psi}{\partial r^2} + \frac{(v_{21} + 2v_{22} - v_{12}) h}{r} \frac{\partial^3 \psi}{\partial r^3} \\
& + v_{22} h \frac{\partial^4 \psi}{\partial r^4} + \frac{1}{r \tan \alpha} \frac{\partial^2 w}{\partial r^2} + \frac{2v_{35} + v_{15}}{r^2} \frac{\partial^3 \phi_1}{\partial r \partial \varphi^2} \\
& + v_{25} \frac{\partial^3 \phi_1}{\partial r^3} + \frac{2v_{25} - v_{15}}{r} \frac{\partial^2 \phi_1}{\partial r^2} + \frac{v_{18}}{r^3} \frac{\partial^3 \phi_2}{\partial \varphi^3} \\
& + \frac{2v_{38} + v_{28}}{r} \frac{\partial^3 \phi_2}{\partial r^2 \partial \varphi} + \frac{2v_{38} - v_{18}}{r} \frac{\partial^2 \phi_2}{\partial r \partial \varphi} + \frac{v_{18}}{r^3} \frac{\partial \phi_2}{\partial \varphi} = 0
\end{aligned} \tag{5}$$

$$\begin{aligned}
& \frac{h}{r \tan \alpha} \frac{\partial^2 \psi}{\partial r^2} - [N_{ax} + N_{axd} \cos(\varpi \tau)] \frac{\partial^2 w}{\partial r^2} \\
& + u_3 \left(\frac{\partial \phi_1}{\partial r} + \frac{\phi_1}{r} \right) + \frac{u_4}{r} \frac{\partial \phi_2}{\partial \varphi} - \rho_1 \frac{\partial^2 w}{\partial \tau^2} = 0
\end{aligned} \tag{6}$$

where, $\rho_1 = h \sum_{k=1}^N \frac{\rho^{(k)}}{N}$ and $-0.5h + (k-1)hN^{-1} \leq z \leq -0.5h$

+ khN^{-1} $k = 1, 2, \dots, N$, in which k is the number of layers, u_{ij} and v_{ij} ($i = 1, 2, 3; j = 1, 2, \dots, 8$), and u_i ($i = 3, 4$) are given in Appendix A. In this study, shear correction factor is not used. The shear stress functions are included in the basic relations as a function of the thickness coordinate. This approach is more realistic, despite the mathematical difficulty in deriving the basic equations (see Appendix A).

The system of Eqs. (3)-(6) can be applied for the PI of MLCCSs.

3. Solution of basic equations

In order to investigate the resonance phenomenon associated with fluctuations in the main form, only the first terms of the series for ψ , w , ϕ_1 , ϕ_2 will be considered. For the MLCCS, which is subjected to freely-supported boundary conditions, the solution of differential equations is sought in the following form (Sofiyev *et al.* 2017, Sofiyev and Kuruoglu 2018)

$$\begin{aligned}
\psi(r, \theta, \tau) &= \bar{\psi}(\tau) \bar{r}^a \sin [\bar{m} \ln \bar{r}] \cos(\bar{n} \varphi) \\
w(r, \theta, \tau) &= \bar{w}(\tau) \bar{r}^a \sin [\bar{m} \ln \bar{r}] \cos(\bar{n} \varphi) \\
\phi_1(r, \theta, \tau) &= \bar{\phi}_1(\tau) \bar{r}^a \cos [\bar{m} \ln \bar{r}] \cos(\bar{n} \varphi) \\
\phi_2(r, \theta, \tau) &= \bar{\phi}_2(\tau) \bar{r}^a \sin [\bar{m} \ln \bar{r}] \sin(\bar{n} \varphi)
\end{aligned} \tag{7}$$

In the above $\psi(\tau)$, $\bar{w}(\tau)$, $\bar{\phi}_1(\tau)$, $\bar{\phi}_2(\tau)$ are the time dependent variables, a is the unknown constant, $\bar{r} = \frac{r}{r_2}$, $r_0 = \frac{r_2}{r_1}$, $\bar{m} = \frac{m\pi}{\ln r_0}$, $\bar{n} = \frac{n}{\sin \alpha}$, in which, m is the half wave number in axial direction and n is the circumferential wave number.

Introducing Eq. (7) into the system of equations from Eq. (3) to Eq. (6) and applying the Galerkin method, we have

$$\begin{aligned}
\eta_{13} \bar{\phi}_1 + \eta_{14} \bar{\phi}_2 - \eta_{12} \bar{w} &= 0 \\
\eta_{23} \bar{\phi}_1 + \eta_{24} \bar{\phi}_2 - \eta_{22} \bar{w} &= 0 \\
\eta_{33} \bar{\phi}_1 + \eta_{34} \bar{\phi}_2 - \eta_{32} \bar{w} + \eta_{31} \bar{\psi} &= 0 \\
\eta_{43} \bar{\phi}_1 + \eta_{44} \bar{\phi}_2 + \lambda_p \frac{d^2 \bar{w}}{d\tau^2} \\
- [N_{ax} + N_{axd} \cos(\varpi \tau)] \lambda_{ax} \bar{w} + \eta_{41} \bar{\psi} &= 0
\end{aligned} \tag{8}$$

where η_{ij} ($i, j = 1, 2, 3, 4$), λ_p and λ_{ax} are given in Appendix B.

Eliminating $\bar{\phi}_0(\tau)$, $\bar{\phi}_1(\tau)$, $\bar{\phi}_2(\tau)$ from the Eq. (8), and after some transformation, we can obtain the following ordinary differential equation of the second order

$$\begin{aligned}
\frac{d^2 \bar{w}(\tau)}{d\tau^2} + \frac{1}{\lambda_p} \left[\frac{\lambda_2 \mu_3 - \lambda_1 \mu_6}{\mu_3} \right. \\
\left. - \lambda_{ax} [N_{ax} + N_{axd} \cos(\varpi \tau)] \right] \bar{w}(\tau) &= 0
\end{aligned} \tag{9}$$

where

$$\lambda_1 = \mu_4 - \frac{\mu_1 \mu_5}{\mu_2}, \quad \lambda_2 = \mu_7 - \frac{\mu_1 \mu_5}{\mu_2} \tag{10}$$

in which

$$\begin{aligned}\mu_1 &= \frac{\eta_{12}\eta_{24}}{\eta_{14}} - \eta_{22}, \mu_2 = \eta_{23} - \frac{\eta_{24}\eta_{13}}{\eta_{14}}, \mu_3 = \eta_{31}, \\ \mu_4 &= \frac{\eta_{12}\eta_{34}}{\eta_{14}} - \eta_{32}, \mu_5 = \eta_{33} - \frac{\eta_{13}\eta_{34}}{\eta_{14}}, \mu_6 = \eta_{41}, \\ \mu_7 &= \frac{\eta_{12}\eta_{44}}{\eta_{14}}, \mu_8 = \eta_{43} - \frac{\eta_{13}\eta_{44}}{\eta_{14}}.\end{aligned}\quad (11)$$

To determine the limits of PIRs, Eq. (9) is converted into the Mathieu-Hill type differential equation (Sofiyev *et al.* 2017)

$$\frac{d^2 \bar{w}(\tau)}{d\tau^2} + \omega^2 [1 - \bar{N}_s - \bar{N}_d \cos(\varpi \tau)] \bar{w}(\tau) = 0 \quad (12)$$

where $\bar{N}_s = N_{ax}/N_{axcrst}^{SDT}$ and $\bar{N}_d = N_{axd}/N_{axcrst}^{SDT}$ denote the static and dynamic axial load factors, ω and N_{axcr}^{SDT} denotes the dimensional frequency and dimensional critical static axial load for the MLCCSs within the FOSDT and are defined as

$$\omega_{SDT} = \sqrt{\frac{\lambda_2 \mu_3 - \lambda_1 \mu_6}{\lambda_{\rho} \mu_3}} \quad (13)$$

and

$$N_{axcrst}^{SDT} = \frac{\lambda_2 \mu_3 - \lambda_1 \mu_6}{\lambda_{ax} \mu_3} \quad (14)$$

In a particular case, as the SDs are not taken into consideration, can be obtained the expressions for the ω_{CST} and N_{axcrst}^{SDT} of MLCCSs within the CST which were presented in the study (Sofiyev and Kuruoglu 2018). Minimizing Eqs. (13) and (14) with wave numbers (m, n), and the parameter, b , we can obtain the minimum values of the critical parameters. The minimum value of the critical axial load for freely-supported LHTOCS within CST and FOSTD is obtained approximately at $b = 2.1$.

The PIRs are formed by periodic solutions of the period T and $2T$, where $T = 2\pi / \varpi$. The PIRs with a period of $2T$ are of practical importance, using the Bolotin's method the solution is given in the form of trigonometric series as (Bolotin 1964)

$$\begin{aligned}\bar{w}(\tau) &= \sum_{p=1,3,5,\dots}^{\infty} [C_p \cos(p\varpi \tau / 2) \\ &\quad + D_p \sin(p\varpi \tau / 2)]\end{aligned}\quad (15)$$

where C_p and D_p are the arbitrary coefficients. If we investigate the vibration at the primary resonance, we may ignore the effects of higher harmonics in the expansion of the above equation and the condition $p = 1$ may be sufficient. After substituting Eq. (15) into Eq. (12) and considering only the first term of the series for the PIRs, and then equating coefficients $\sin(\varpi \tau / 2)$ and $\cos(\varpi \tau / 2)$ Eq. (12) reduce to

$$\begin{aligned}[-\varpi^2 + 4\omega^2(1 - \bar{N}_s - \bar{N}_d / 2)]C_1 \cos(\varpi \tau / 2) \\ + [-\varpi^2 + 4\omega^2(1 - \bar{N}_s + \bar{N}_d / 2)]D_1 \sin(\varpi \tau / 2) = 0\end{aligned}\quad (16)$$

Table 1 Comparison of the magnitudes of origin of borders of LO cylinders with (90/0/90) lay-up versus L_1/R

	Ng and Lam (1999)	Present study
L_1/R	$\varpi_{11} = \varpi_{12}$	$\varpi_{11} = \varpi_{12}$
2.0	93.582	93.512
2.2	89.527	86.863

When $C_1 \neq 0$ and $D_1 \neq 0$, from Eq. (16), we obtain the formula for left and right borders of PIRs for MLCCSs within the FOSDT

$$\varpi_{1j} = 2\omega \sqrt{1 - \bar{N}_s \mp 0.5\bar{N}_d}, \quad (j=1,2) \quad (17)$$

where ϖ_{11} and ϖ_{12} are denote left and right borders of PIRs for MLCCSs based on the FOSDT for certain mode (m, n). The left and right limits of dimensionless PIRs for MLCCSs based on the FOSDT, i.e., ϖ_{1j} , are defined as

$$\tilde{\varpi}_{1j} = 2\pi r_1 \varpi_{1j} \sqrt{\frac{[1 - (\nu_{12}^{(k)})^2] \rho^{(k)}}{E_{11}^{(k)}}}, \quad (j=1,2) \quad (18)$$

When $\bar{N}_d = 0$, from the Eq. (18), the formula for the point of origin of left and right borders is found.

4. Results and discussion

4.1 Comparative examples

Example 1:

To confirm the present study, the values of the beginning of the main PIRs of the laminated orthotropic (LO) cylindrical shell with packing (90/0/90) are compared with the values obtained in Ng and Lam (1999), which is based on Donnell's shell theories in the CST (see Table 1). As $\alpha \rightarrow 0^\circ$ is considered in the Eq. (18), the formula for MLCCS is converted to an expression for LO cylindrical shells. The parameters used in calculations are: $h/r = 0.005$, $E_{11}^{(k)}/E_{22}^{(k)} = 40$, $G_{12}^{(k)}/E_{22}^{(k)} = 0.5$, $\nu_{12}^{(k)} = 0.25$ and $\rho^{(k)} = 1$ (Ng and Lam 1999), and $k = 2$, and $\bar{N}_s = 0.1$. Here L_1 and R are the length and radius of the cylindrical shell, respectively. Our study gives acceptable results in comparison with the result presented in Ng and Lam (1999).

Example 2:

The values of $\omega_{1SDT} = \omega_{SDT} (0.1L^2 h^{-1}) \sqrt{\rho^{(k)}/E_{22}^{(k)}}$ ($k = 3$ and 4) for the LO cylindrical shells with (0/90/0) and (0/90/90/0) lay-up are compared with the results of Ferreira *et al.* (2011) who use a radial basis function, while Reddy and Liu (1985) use FOSDT and HOSDT (Table 2). In present study the shear stress shape functions are considered as $f_1^{(k)}(z) = f_2^{(k)}(z) = h \sinh(zh^{-1}) - z \cosh(2^{-1})$. The geometries of the LO cylindrical shell are, $L_1 R^{-1} = 0.2$ and $L_1 h^{-1} = 10$. Here $\alpha \rightarrow 0^\circ$ is taken into account in the Eq. (13). The material constants are, $E_{11}^{(k)}/E_{22}^{(k)} = 25$,

Table 2 Comparison of the ω_1 for LO cylindrical shells with (0/90/0) and (0/90/90/0) lay-up

Lay-up	$\omega_{1SDT}, (n)$	
	(0/90/0)	(0/90/90/0)
Reddy and Liu (1985) FOSDST	12.207	12.267
Reddy and Liu (1985) HOSDST	11.85	11.830
Ferreira <i>et al.</i> (2011)	11.923	11.901
Present study	12.017(8)	11.760(8)

$G_{23}^{(k)}/E_{22}^{(k)} = 0.2$, $G_{12}^{(k)}/E_{22}^{(k)} = G_{13}^{(k)}/E_{22}^{(k)} = 0.5$, $v_{12}^{(k)} = 0.25$, $v_{21}^{(k)} = v_{12}^{(k)} E_{22}^{(k)}/E_{11}^{(k)}$ and $\rho^{(k)} = 1 \text{ kg/m}^3$, are given in the Reddy and Liu (1985), and Ferreira *et al.* (2011). Table 2 shows a good agreement between the current results and the results of Reddy and Liu (1985), and Ferreira *et al.* (2011).

4.2 Variation of the values of borders of PIRs for MLCCSs based on the FOSDT

After proposing explicit analytical expressions for borders of PIRs of MLCCSs with several lamination schemes, the new results are presented in this section. For each case, four different lamination schemes are provided: (0/90/0), (90/0/90), (0/90/90/0) and (90/0/0/90). In each case, the total thickness of the MLCCS, $h = 0.01 \text{ m}$.

It is assumed that the material of the lamina is boron-epoxy composites with the following orthotropic properties (Reddy 2004)

$$\begin{aligned}
 E_{11}^{(k)} &= 2.069 \times 10^{11} \text{ Pa}, & E_{22}^{(k)} &= E_{11}^{(k)}/10 \text{ Pa}, \\
 G_{23}^{(k)} &= 4.14 \times 10^9 \text{ Pa}, & G_{12}^{(k)} &= G_{13}^{(k)} = 6.9 \times 10^9 \text{ Pa}, \\
 v_{21}^{(k)} &= v_{12}^{(k)} E_{22}^{(k)}/E_{11}^{(k)}, & v_{12}^{(k)} &= 0.3 \\
 \text{and } \rho^{(k)} &= 1950 \text{ kg/m}^3.
 \end{aligned}$$

Table 3 Variation of the values of left and right borders of PIRs $\tilde{\omega}_{1j}$ ($j = 1, 2$) for MLCCSs versus the \bar{N}_d for different $\bar{N}_{\alpha x}$

\bar{N}_s	\bar{N}_d	(0/90/0)				(90/0/90)			
		CST		FOSDT		CST		FOSDT	
		$\tilde{\omega}_{11}$	$\tilde{\omega}_{12}$	$\tilde{\omega}_{11}$	$\tilde{\omega}_{12}$	$\tilde{\omega}_{11}$	$\tilde{\omega}_{12}$	$\tilde{\omega}_{11}$	$\tilde{\omega}_{12}$
0.1	0	34.962	34.962	23.605	23.605	14.394	14.394	13.446	13.446
	0.2	34.873	35.050	23.473	23.736	14.324	14.464	13.371	13.521
	0.4	34.784	35.138	23.341	23.866	14.254	14.533	13.296	13.595
	0.6	34.695	35.226	23.208	23.995	14.184	14.602	13.220	13.669
0.3	0	33.144	33.144	20.818	20.818	12.924	12.924	11.859	11.859
	0.2	32.862	33.423	20.367	21.259	12.688	13.155	11.602	12.110
	0.4	32.579	33.699	19.905	21.691	12.449	13.382	11.339	12.356
	0.6	32.292	33.974	19.433	22.115	12.204	13.605	11.070	12.598
0.5	0	31.220	31.220	17.594	17.594	11.262	11.262	10.022	10.022
	0.2	30.720	31.712	16.691	18.453	10.807	11.700	9.508	10.511
	0.4	30.212	32.196	15.737	19.273	10.332	12.122	8.964	10.979
	0.6	29.696	32.673	14.720	20.060	9.834	12.529	8.385	11.427
\bar{N}_s	\bar{N}_d	(0/90/90/0)				(90/0/0/90)			
0.1	0	33.604	33.604	23.395	23.395	17.224	17.224	15.338	15.338
	0.2	33.514	33.695	23.265	23.525	17.148	17.300	15.253	15.423
	0.4	33.423	33.785	23.134	23.654	17.072	17.375	15.167	15.508
	0.6	33.332	33.875	23.002	23.782	16.995	17.451	15.081	15.592
0.3	0	31.743	31.743	20.633	20.633	15.633	15.633	13.527	13.527
	0.2	31.454	32.029	20.186	21.070	15.380	15.882	13.234	13.814
	0.4	31.163	32.313	19.729	21.499	15.123	16.127	12.934	14.095
	0.6	30.869	32.594	19.261	21.919	14.862	16.368	12.628	14.370
0.5	0	29.765	29.765	17.438	17.438	13.861	13.861	11.433	11.433
	0.2	29.250	30.272	16.543	18.289	13.381	14.324	10.846	11.991
	0.4	28.726	30.770	15.597	19.102	12.883	14.774	10.226	12.524
	0.6	28.191	31.260	14.590	19.882	12.366	15.209	9.565	13.035

Table 4 Variation of the values of left and right borders of PIRs $\tilde{\omega}_{1j}$ ($j = 1, 2$) for MLCCSs versus the \bar{N}_d for different α

α	\bar{N}_d	(0/90/0)				(90/0/90)			
		CST		FOSDT		CST		FOSDT	
		$\tilde{\omega}_{11}$	$\tilde{\omega}_{12}$	$\tilde{\omega}_{11}$	$\tilde{\omega}_{12}$	$\tilde{\omega}_{11}$	$\tilde{\omega}_{12}$	$\tilde{\omega}_{11}$	$\tilde{\omega}_{12}$
0	0	35.215	35.215	23.867	23.867	14.971	14.971	14.043	14.043
	0.2	35.170	35.260	23.801	23.933	14.935	15.008	14.004	14.082
	0.4	35.080	35.349	23.668	24.065	14.861	15.081	13.926	14.160
	0.6	34.989	35.439	23.533	24.197	14.787	15.153	13.847	14.237
30	0	34.962	34.962	23.605	23.605	14.394	14.394	13.446	13.446
	0.2	34.917	35.006	23.539	23.670	14.359	14.429	13.409	13.484
	0.4	34.829	35.094	23.407	23.801	14.289	14.499	13.334	13.558
	0.6	34.740	35.182	23.275	23.930	14.219	14.568	13.258	13.632
60	0	34.527	34.527	23.231	23.231	13.398	13.398	12.429	12.429
	0.2	34.483	34.570	23.166	23.295	13.366	13.430	12.394	12.464
	0.4	34.396	34.657	23.036	23.423	13.301	13.493	12.325	12.532
	0.6	34.309	34.743	22.906	23.551	13.237	13.557	12.255	12.600
α	\bar{N}_d	(0/90/90/0)				(90/0/0/90)			
0	0	33.897	33.897	23.714	23.714	17.667	17.667	15.806	15.806
	0.2	33.851	33.943	23.648	23.779	17.627	17.706	15.762	15.850
	0.4	33.758	34.035	23.515	23.910	17.549	17.784	15.674	15.938
	0.6	33.666	34.127	23.382	24.041	17.469	17.862	15.585	16.024
30	0	33.604	33.604	23.395	23.395	17.224	17.224	15.338	15.338
	0.2	33.559	33.649	23.330	23.460	17.186	17.262	15.296	15.381
	0.4	33.468	33.740	23.200	23.590	17.110	17.338	15.210	15.466
	0.6	33.377	33.830	23.068	23.718	17.034	17.413	15.124	15.550
60	0	33.098	33.098	22.917	22.917	16.483	16.483	14.580	14.580
	0.2	33.054	33.142	22.853	22.980	16.447	16.519	14.540	14.621
	0.4	32.966	33.230	22.725	23.107	16.375	16.590	14.458	14.701
	0.6	32.877	33.318	22.596	23.233	16.303	16.661	14.376	14.781

The variation of the values of left and right borders of PIRs ($\tilde{\omega}_{1j}$ ($j = 1, 2$)) for MLCCSs with laminations (0/90/0), (90/0/90), (0/90/90/0) and (90/0/0/90) versus the \bar{N}_d based on the CST and FOSDT for different \bar{N}_s are reflected in Table 3. The following data are considered in the computations: $h/R_1 = 0.04$, $R_1/L = 5$, $\alpha = 30^\circ$ and $(m, n) = (1, 3)$. The borders of PIRs for MLCCSs based on the CST and FOSDT diminish, as \bar{N}_s increment. The left borders values of PIRs ($\tilde{\omega}_{11}$) for MLCCSs diminish, whereas, the right borders values of PIRs ($\tilde{\omega}_{12}$) increment, when the \bar{N}_d increment from zero to 0.6. It should be noted that the area between the borders decreases, as the static axial load coefficient increment. When $\bar{N}_d = 0$ and \bar{N}_s increases from 0.1 to 0.5, the effects of shear deformations (SDs) on the $\tilde{\omega}_{11}$ increase from (-32.48%) to (-43.65%). When $\bar{N}_s = 0.1$ and \bar{N}_d increases from 0 to 0.6, the effects of SDs on the left limits of PIRs increase slightly, whereas these effects on the $\tilde{\omega}_{11}$ are important and increase from (-43.65%) to 50.43%, from (-11.01%) to 14.73%, from (-41.41%) to (-48.25%) and from (-17.52%) to (-22.65%)

with laminations (0/90/0), (90/0/90), (0/90/90/0) and (90/0/0/90) conical shells, respectively, when $\bar{N}_s = 0.5$ and \bar{N}_d increases from 0 to 0.6. The effects of SDs on the right border of the PIRs are weakly reduced, when $\bar{N}_s = 0.1$ and \bar{N}_d increases from 0 to 0.6, whereas these effects significantly reduced when \bar{N}_d increases for large \bar{N}_s . For example, when $\bar{N}_s = 0.5$ and \bar{N}_d increases from 0 to 0.6, these effects reduced from (-43.65%) to (-38.6%), from (-11.01%) to (-8.8%), from (-41.41%) to (-36.4%) and from (-17.52%) to (-14.29%) for laminations (0/90/0), (90/0/90), (0/90/90/0) and (90/0/0/90), respectively.

The variations of left and right borders of PIRs ($\tilde{\omega}_{1j}$ ($j = 1, 2$)) for MLCCSs with laminations (0/90/0), (90/0/90), (0/90/90/0) and (90/0/0/90) based on the CST and FOSDT, versus the \bar{N}_d for different R_1/h ratio, are reflected in Table 4, and Figs. 2 and 3. The MLCCS and load parameters are considered as $L/R_1 = 2$, $\alpha = 30^\circ$, $\bar{N}_s = 0.2$ and $(m, n) = (1, 4)$. Based on the CST and FOSDT, the values of $\tilde{\omega}_{1j}$ ($j = 1, 2$) for MLCCSs with (0/90/0) and (0/90/90/0) lay-up decrease (Fig. 2), while those for

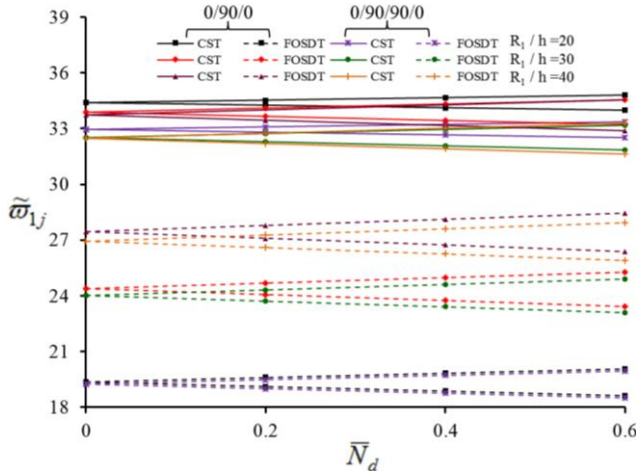


Fig. 2 Distribution of the magnitudes of left and right borders of PIRs for MLCCSs with (0/90/0) and (0/90/90/0) lay-up versus the \bar{N}_d for different R_1/h

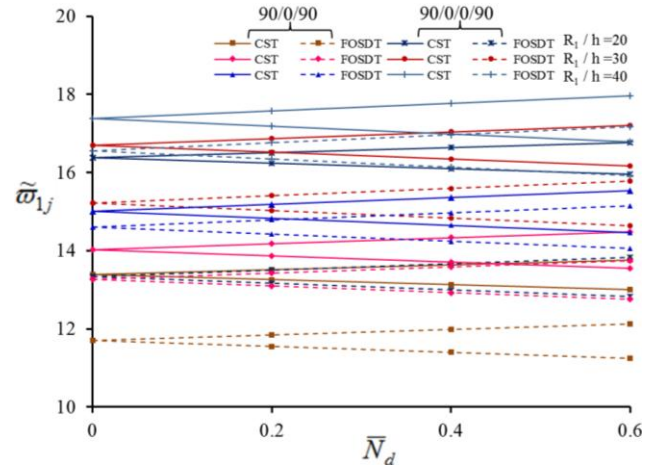


Fig. 3 Distribution of the magnitudes of left and right borders of PIRs for MLCCSs with (90/0/90) and (90/0/0/90) lay-up versus the \bar{N}_d for different R_1/h

Table 5 Variation of the values of left and right borders of PIRs for MLCCSs versus the \bar{N}_d for different L/R_1

		(0/90/0)				(90/0/90)			
		CST		FOSDT		CST		FOSDT	
L/R_1	\bar{N}_d	\tilde{w}_{11}	\tilde{w}_{12}	\tilde{w}_{11}	\tilde{w}_{12}	\tilde{w}_{11}	\tilde{w}_{12}	\tilde{w}_{11}	\tilde{w}_{12}
0.2	0	34.259	34.259	22.505	22.505	14.359	14.359	13.444	13.444
	0.1	34.167	34.352	22.364	22.646	14.280	14.438	13.360	13.528
	0.3	33.981	34.535	22.079	22.923	14.121	14.593	13.189	13.694
	0.5	33.794	34.718	21.791	23.198	13.960	14.747	13.017	13.858
0.3	0	35.321	35.321	28.772	28.772	19.423	19.423	19.097	19.097
	0.1	35.174	35.467	28.591	28.951	19.305	19.540	18.977	19.216
	0.3	34.879	35.758	28.227	29.306	19.067	19.772	18.735	19.451
	0.5	34.581	36.046	27.858	29.657	18.827	20.001	18.490	19.684
0.4	0	38.321	38.321	34.568	34.568	26.377	26.377	26.237	26.237
	0.1	38.126	38.516	34.351	34.784	26.213	26.539	26.072	26.400
	0.3	37.732	38.902	33.914	35.210	25.883	26.862	25.740	26.724
	0.5	37.334	39.284	33.471	35.632	25.548	27.180	25.403	27.044
L/R_1	\bar{N}_d	(0/90/90/0)				(90/0/0/90)			
0.2	0	32.964	32.964	22.428	22.428	16.876	16.876	14.974	14.974
	0.1	32.868	33.059	22.288	22.568	16.793	16.959	14.880	15.068
	0.3	32.676	33.249	22.004	22.845	16.625	17.123	14.691	15.252
	0.5	32.483	33.437	21.716	23.118	16.455	17.286	14.499	15.435
0.3	0	34.529	34.529	28.850	28.850	20.764	20.764	20.010	20.010
	0.1	34.378	34.679	28.669	29.030	20.643	20.884	19.884	20.134
	0.3	34.074	34.978	28.304	29.386	20.399	21.122	19.631	20.381
	0.5	33.767	35.274	27.934	29.738	20.152	21.358	19.374	20.625
0.4	0	38.152	38.152	34.984	34.984	26.850	26.850	26.513	26.513
	0.1	37.951	38.352	34.764	35.202	26.686	27.013	26.347	26.678
	0.3	37.546	38.749	34.321	35.634	26.354	27.336	26.011	27.006
	0.5	37.136	39.142	33.873	36.060	26.019	27.656	25.671	27.329

MLCCSs with (90/0/90) and (90/0/0/90) lay-up increase, as R_1/h increment (see, Fig. 3). As the effects of lamination schemes (90/0/90), (0/90/90/0) and (90/0/0/90) on the values of borders of PIRs ($\tilde{\omega}_{1j}$ ($j = 1, 2$)) for MLCCS based on FOSDT are compared to the (0/90/0) laminated shells, the greatest effect is observed in the conical shell with the lay-up (90/0/90), the smallest effect is observed in the shell with the lay-up (0/90/90/0), and this difference decreases due to the increase in the ratio R_1/h . When \bar{N}_d ($= 0.4$) is kept constant, the effects of SDs on the $\tilde{\omega}_{1j}$ ($j = 1, 2$) are significant and decrease, when the ratio R_1/h increases from 20 to 40. Moreover, these effects change in accordance with the number and sequence of layers. For example, the SDs effects on the $\tilde{\omega}_{11}$ reduce from about (−44.66%) to (−19.31%), from (−13.16%) to (−2.81%), from (−42.56%) to (−17.67%) and from (−19.29%) to (−4.98%) and SDs effects on the $\tilde{\omega}_{12}$ also reduce from (−42.74%) to (−17.94%), from (−12.13%) to (−2.55%), from (−40.64%) to (−16.38%) and from (−17.92%) to (−4.54%) for (0/90/0), (90/0/90), (0/90/90/0) and

(90/0/0/90) lay-up, respectively, when the ratio R_1/h increases from 20 to 40.

Table 5 aims to analyze the effect of L/R_1 on the values of boundaries of PIRs, $\tilde{\omega}_{1j}$ ($j = 1, 2$), for MLCCSs with (0/90/0), (90/0/90), (0/90/90/0) and (90/0/0/90) lay-up for $\bar{N}_d = 0, 0.1, 0.3, 0.5$, based on the CST and FOSDT. Here, the following data are considered: $L/R_1 = 0.2, 0.4, 0.6$, $h/R_1 = 0.04$, $\alpha = \pi/12$, $N_s = 0.2$ and $(m, n) = (1, 2)$. It is worth nothing that values of $\tilde{\omega}_{1j}$ ($j = 1, 2$) for MLCCSs with all lay-up increase, as L/R_1 increasing from 0.2 to 0.4. It can be seen that this increment is more evident in MLCCSs with the packing (90/0/90) or (90/0/0/90) than in casings with the (0/90/0) or (0/90/90/0) stowage. When \bar{N}_d ($= 0.5$) is kept constant, the effects of SDs on the $\tilde{\omega}_{1j}$ ($j = 1, 2$) are significant and reduce, as the ratio L/R_1 increases from 0.2 to 0.4. In addition, these effects change in accordance with the number and sequence of layers. For example, effects of SDs on the $\tilde{\omega}_{11}$ reduce from (−35.52%) to (−10.35%), from (−6.76%) to (−0.57%), from (−33.15%) to (−8.79%) and from (−11.89%) to (−1.34%) and these influences on

Table 6 Variation of the values of left and right borders of PIRs of MLCCSs versus the \bar{N}_d for different α

L/R_1	\bar{N}_d	(0/90/0)				(90/0/90)			
		CST		FOSDT		CST		FOSDT	
		$\tilde{\omega}_{11}$	$\tilde{\omega}_{12}$	$\tilde{\omega}_{11}$	$\tilde{\omega}_{12}$	$\tilde{\omega}_{11}$	$\tilde{\omega}_{12}$	$\tilde{\omega}_{11}$	$\tilde{\omega}_{12}$
0.2	0	34.259	34.259	22.505	22.505	14.359	14.359	13.444	13.444
	0.1	34.167	34.352	22.364	22.646	14.280	14.438	13.360	13.528
	0.3	33.981	34.535	22.079	22.923	14.121	14.593	13.189	13.694
	0.5	33.794	34.718	21.791	23.198	13.960	14.747	13.017	13.858
0.3	0	35.321	35.321	28.772	28.772	19.423	19.423	19.097	19.097
	0.1	35.174	35.467	28.591	28.951	19.305	19.540	18.977	19.216
	0.3	34.879	35.758	28.227	29.306	19.067	19.772	18.735	19.451
	0.5	34.581	36.046	27.858	29.657	18.827	20.001	18.490	19.684
0.4	0	38.321	38.321	34.568	34.568	26.377	26.377	26.237	26.237
	0.1	38.126	38.516	34.351	34.784	26.213	26.539	26.072	26.400
	0.3	37.732	38.902	33.914	35.210	25.883	26.862	25.740	26.724
	0.5	37.334	39.284	33.471	35.632	25.548	27.180	25.403	27.044
L/R_1	\bar{N}_d	(0/90/90/0)				(90/0/0/90)			
0.2	0	32.964	32.964	22.428	22.428	16.876	16.876	14.974	14.974
	0.1	32.868	33.059	22.288	22.568	16.793	16.959	14.880	15.068
	0.3	32.676	33.249	22.004	22.845	16.625	17.123	14.691	15.252
	0.5	32.483	33.437	21.716	23.118	16.455	17.286	14.499	15.435
0.3	0	34.529	34.529	28.850	28.850	20.764	20.764	20.010	20.010
	0.1	34.378	34.679	28.669	29.030	20.643	20.884	19.884	20.134
	0.3	34.074	34.978	28.304	29.386	20.399	21.122	19.631	20.381
	0.5	33.767	35.274	27.934	29.738	20.152	21.358	19.374	20.625
0.4	0	38.152	38.152	34.984	34.984	26.850	26.850	26.513	26.513
	0.1	37.951	38.352	34.764	35.202	26.686	27.013	26.347	26.678
	0.3	37.546	38.749	34.321	35.634	26.354	27.336	26.011	27.006
	0.5	37.136	39.142	33.873	36.060	26.019	27.656	25.671	27.329

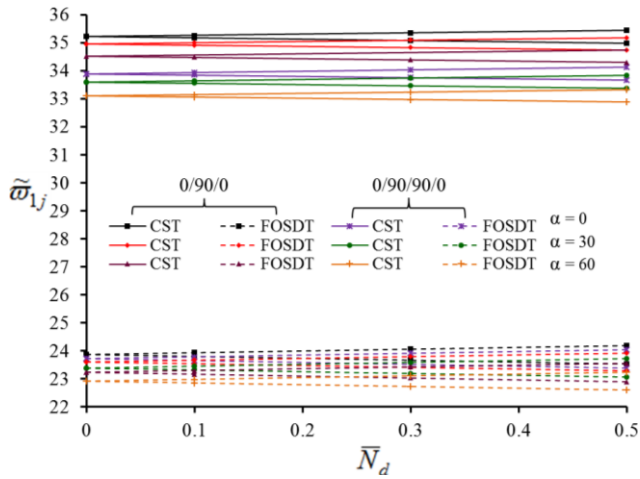


Fig. 4 Distribution of the magnitudes of left and right borders of PIRs for MLCCSs with (0/90/0) and (0/90/90/0) lay-up versus the \bar{N}_d for different semi-vertex angle, α

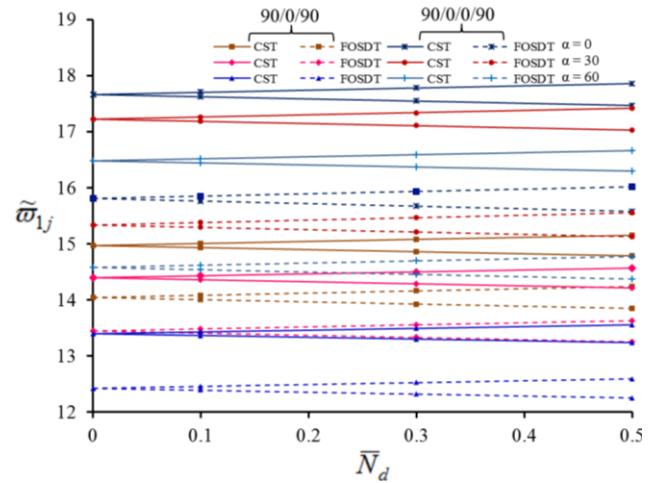


Fig. 5 Distribution of the magnitudes of left and right borders of PIRs for MLCCSs with (90/0/90) and (90/0/0/90) lay-up versus the \bar{N}_d for different semi-vertex angle, α

Table 7 Variation of the values of left and right limits of PIRs for MLCCSs versus the \bar{N}_d for different (m, n)

		(0/90/0)				(90/0/90)			
		CST		FOSDT		CST		FOSDT	
(m, n)	\bar{N}_d	$\tilde{\omega}_{11}$	$\tilde{\omega}_{12}$	$\tilde{\omega}_{11}$	$\tilde{\omega}_{12}$	$\tilde{\omega}_{11}$	$\tilde{\omega}_{12}$	$\tilde{\omega}_{11}$	$\tilde{\omega}_{12}$
(1,2)	0	34.973	34.973	23.686	23.686	14.631	14.631	13.753	13.753
	0.1	34.928	35.018	23.620	23.752	14.595	14.667	13.715	13.791
	0.3	34.839	35.106	23.488	23.883	14.523	14.738	13.638	13.867
	0.5	34.750	35.195	23.355	24.013	14.450	14.809	13.561	13.943
(2,2)	0	139.681	139.681	57.039	57.039	51.484	51.484	39.345	39.345
	0.1	139.616	139.746	56.880	57.197	51.401	51.568	39.236	39.454
	0.3	139.487	139.875	56.562	57.512	51.233	51.734	39.016	39.672
	0.5	139.357	140.004	56.241	57.826	51.065	51.900	38.795	39.888
(3,2)	0	315.290	315.290	89.801	89.801	115.669	115.669	71.073	71.073
	0.1	315.219	315.361	89.551	90.050	115.547	115.790	70.876	71.271
	0.3	315.077	315.504	89.050	90.546	115.304	116.032	70.479	71.663
	0.5	314.935	315.645	88.545	91.040	115.060	116.274	70.079	72.054
(m, n)	\bar{N}_d	(0/90/90/0)				(90/0/0/90)			
(1,2)	0	33.897	33.897	23.714	23.714	17.667	17.667	15.806	15.806
	0.1	33.851	33.943	23.648	23.779	17.627	17.706	15.762	15.850
	0.3	33.758	34.035	23.515	23.910	17.549	17.784	15.674	15.938
	0.5	33.666	34.127	23.382	24.041	17.469	17.862	15.585	16.024
(2,2)	0	33.604	33.604	23.395	23.395	17.224	17.224	15.338	15.338
	0.1	33.559	33.649	23.330	23.460	17.186	17.262	15.296	15.381
	0.3	33.468	33.740	23.200	23.590	17.110	17.338	15.210	15.466
	0.5	33.377	33.830	23.068	23.718	17.034	17.413	15.124	15.550
(3,2)	0	33.098	33.098	22.917	22.917	16.483	16.483	14.580	14.580
	0.1	33.054	33.142	22.853	22.980	16.447	16.519	14.540	14.621
	0.3	32.966	33.230	22.725	23.107	16.375	16.590	14.458	14.701
	0.5	32.877	33.318	22.596	23.233	16.303	16.661	14.376	14.781

the $\tilde{\omega}_{12}$ also reduce from (-33.18%) to (-9.3%) , from (-6.03%) to (-0.5%) , from (-30.86%) to (-7.87%) and from (-10.71%) to (-1.18%) for $(0/90/0)$, $(90/0/90)$, $(0/90/90/0)$ and $(90/0/0/90)$ lay-up, respectively, as the ratio, R_1/h , increases from 20 to 40.

Table 6 and Figs. 4 and 5, shows the influence of the semi-vertex angle, α , on the values of boundaries of PIRs of MLCCSs with $(0/90/0)$, $(90/0/90)$, $(0/90/90/0)$ and $(90/0/0/90)$ lay-up for fixed $\bar{N}_d = 0, 0.1, 0.3, 0.5$, based on the CST and FOSDT. In this example, the following geometric and physical parameters are considered: $\alpha = 0^\circ, 30^\circ, 60^\circ$, $h/R_1 = 0.04$, $L/R_1 = 0.2$, $\bar{N}_s = 0.1$ and $(m, n) = (1, 3)$. It can be argued that with increasing the semi-vertex angle, α , from 0° to 60° , the values of boundaries of PIRs for MLCCSs with four lay-up, based on the CST and FOSDT reduce. The values for $\alpha = 0^\circ$ belong to the cylinder. When $\bar{N}_d (= 0.3)$ is kept constant, the effects of SDs on the $\tilde{\omega}_{1j}$ ($j = 1, 2$) are significant and increase, when the semi-vertex angle, α , increases from 0° to 60° . In addition, these effects change in accordance with the number and sequence of layers and the following percentages appear: the effects of SDs on the $\tilde{\omega}_{11}$ increase from (-32.53%) to (-33.03%) , from (-6.29%) to (-7.34%) , from (-30.34%) to (-31.07%) and from (-11.89%) to (-12.34%) and these effects on the $\tilde{\omega}_{12}$ also increment from (-31.92%) to (-32.41%) , from (-6.11%) to (-7.12%) , from (-29.75%) to (-30.46%) and from (-10.38%) to (-11.39%) for the lay-up $(0/90/0)$, $(90/0/90)$, $(0/90/90/0)$ and $(90/0/0/90)$, respectively, when the semi-vertex angle, α , increases from 0° to 60° (see, Figs. 4 and 5, also).

The variation of the values of left and right borders of PIRs for MLCCSs versus the \bar{N}_d for different meridional wave number, m , and for the $(0/90/0)$, $(90/0/90)$, $(0/90/90/0)$ and $(90/0/0/90)$ lay-up, are tabulated in Table 7. The calculations data are, $\bar{N}_s = 0.1$, $R_1/h = 25$, $L/R_1 = 0.2$, $\alpha = 30^\circ$, $n = 2$. The magnitudes of left and right borders of PIRs for MLCCSs with the entire stacking are clearly increasing, with an increase of m from 1 to 3 for the fixed n ($n = 2$). As $\bar{N}_d (= 0.5)$ is kept constant, the influences of SDs on the magnitudes of left and right limits of PIRs for MLCCSs obviously increase with the increasing of meridional wave number, m , from 1 to 3. For instance, the following percentages appear for SDs influences; the effects of SDs on the ω_{11} increase from (-34.77%) to (-73.19%) , from (-6.6%) to (-40.51%) , from (-32.65%) to (-71.98%) and from (-11.22%) to (-49.92%) and these effects on the ω_{12} also increment from (-33.73%) to (-72.49%) , from (-6.28%) to (-39.45%) , from (-31.64%) to (-71.25%) and from (-10.7%) to (-48.87%) for lay-up $(0/90/0)$, $(90/0/90)$, $(0/90/90/0)$ and $(90/0/0/90)$, respectively, when the meridional wave number, m , increases from 1 to 3. As can be seen from these “percentages”, such effects vary depending on the number and order of layers.

5. Conclusions

The PI of MLCCSs subjected to axial load periodically varying the time, using FOSDT is studied. Based on the physical and mathematical reasoning, the basic equations

for MLCCS are derived and then the Galerkin method is used to obtain the ordinary differential equation of the motion. The equation of motion converted to the Mathieu-Hill type differential equation, in which the PI is examined employing the Bolotin's method. In order to prove the validity of the formulas, present results are compared with the results of other studies in the literature. Finally, the influences of various parameters such as lay-up, SDs, aspect ratio, as well as loading factors on the limits of the PIRs of MLCCSs are examined.

References

- Alankaya, V. and Oktem, A.S. (2016), “Static analysis of laminated and sandwich composite doubly-curved shallow shells”, *Steel Compos. Struct., Int. J.*, **20**(5), 1043-1066.
- Ambartsumian, S.A. (1961), *Theory of Anisotropic Shells*, State Publishing House for Physical and Mathematical Literature, Moscow, Russia.
- Argento, A. and Scott, R. (1993), “Dynamic Instability Of Layered Anisotropic Circular Cylindrical Shells, Part I: Theoretical Development”, *J. Sound Vib.*, **162**(2), 311-322.
- Avramov, K., Papazov, S. and Breslavsky, I. (2017), “Dynamic instability of shallow shells in three-dimensional incompressible inviscid potential flow”, *J. Sound Vib.*, **394**, 593-611.
- Awrejcewicz, J., Kurpa, L. and Mazur, O. (2016), “Dynamical instability of laminated plates with external cutout”, *Int. J. Non-Linear Mech.*, **81**, 103-114.
- Biswal, M., Sahu, S.K., Asha, A.V. and Nanda, N. (2016), “Hygrothermal effects on buckling of composite shell-experimental and FEM results”, *Steel Compos. Struct., Int. J.*, **22**(6), 1445-1463.
- Biswal, M., Sahu, S. and Asha, A. (2017), “Dynamic stability of woven fiber laminated composite shallow shells in hygrothermal environment”, *Int. J. Struct. Stabil. Dyn.*, **17**(8), 1750084.
- Bolotin, V.V. (1964), *Dynamic Stability of Elastic Systems*, Holden-Day, San Francisco, CA, USA.
- Brischetto, S., Tornabene, F., Fantuzzi, N. and Baccocchi, M. (2017), “Interpretation of boundary conditions in the analytical and numerical shell solutions for mode analysis of multilayered structures”, *Int. J. Mech. Sci.*, **122**, 18-28.
- Caliri Jr., M.F., Ferreira, A.J. and Tita, V. (2017), “A new finite element for thick laminates and sandwich structures using a generalized and unified plate theory”, *Int. J. Numer. Methods Eng.*, **109**(2), 290-304.
- Darabi, M. and Ganesan, R. (2016), “Non-linear dynamic instability analysis of laminated composite cylindrical shells subjected to periodic axial loads”, *Compos. Struct.*, **147**, 168-184.
- Darabi, M. and Ganesan, R. (2017), “Non-linear vibration and dynamic instability of internally-thickness-tapered composite plates under parametric excitation”, *Compos. Struct.*, **176**, 82-104.
- Dey, T. and Ramachandra, L. (2014), “Static and dynamic instability analysis of composite cylindrical shell panels subjected to partial edge loading”, *Int. J. Non-Linear Mech.*, **64**, 46-56.
- Fazilati, J. and Ovesy, H. (2010), “Dynamic instability analysis of composite laminated thin-walled structures using two versions of FSM”, *Compos. Struct.*, **92**(9), 2060-2065.
- Ferreira, A., Carrera, E., Cinefra, M., Roque, C. and Polit, O. (2011), “Analysis of laminated shells by a sinusoidal shear deformation theory and radial basis functions collocation, accounting for through-the-thickness deformations”, *Compos.*

- Part B: Eng.*, **42**(5), 1276-1284.
- Ferreira, A., Carrera, E., Cinefra, M. and Zenkour, A. (2016), "A radial basis functions solution for the analysis of laminated doubly-curved shells by a Reissner-Mixed Variational Theorem", *Mech. Adv. Mater. Struct.*, **23**(9), 1068-1079.
- Ganapathi, M. and Balamurugan, V. (1998), "Dynamic instability analysis of a laminated composite circular cylindrical shell", *Comput. Struct.*, **69**(2), 181-189.
- Goroshko, O. and Emel'yanenko, V. (1975), "Dynamic stability of layered anisotropic shells", *Soviet Appl. Mech.*, **11**(7), 720-725.
- Hu, H.-T. and Chen, H.C. (2018), "Buckling optimization of laminated truncated conical shells subjected to external hydrostatic compression", *Compos. Part B: Eng.*, **135**, 95-109.
- Hui, D. (1985), "Asymmetric postbuckling of symmetrically laminated cross-ply, short cylindrical panels under compression", *Compos. Struct.*, **3**(1), 81-95.
- Khayat, M., Poorveis, D. and Moradi, S. (2016), "Buckling analysis of laminated composite cylindrical shell subjected to lateral displacement-dependent pressure using semi-analytical finite strip method", *Steel Compos. Struct., Int. J.*, **22**(2), 301-321.
- Khayat, M., Poorveis, D. and Moradi, S. (2017), "Buckling analysis of functionally graded truncated conical shells under external displacement-dependent pressure", *Steel Compos. Struct., Int. J.*, **23**(1), 1-16.
- Kumar, L.R., Datta, P. and Prabhakara, D. (2005), "Dynamic instability characteristics of laminated composite doubly curved panels subjected to partially distributed follower edge loading", *Int. J. Solids Struct.*, **42**(8), 2243-2264.
- Laoufi, I., Ameer, M., Zidi, M., Bedia, E.A.A. and Bousahla, A.A. (2016), "Mechanical and hygrothermal behaviour of functionally graded plates using a hyperbolic shear deformation theory", *Steel Compos. Struct., Int. J.*, **20**(4), 889-911.
- Liao, C.L. and Cheng, C.R. (1994), "Dynamic Stability Of Stiffened Laminated Composite Plates And Shells Subjected To In-Plane Pulsating Forces", *J. Sound Vib.*, **174**, 335-351.
- Ma, Y., Cheng, X., Wang, Z., Guo, X., Zhang, J. and Xu, Y. (2018), "Buckling and post-buckling behaviors of 1/3 composite cylindrical shell with an opening", *Steel Compos. Struct., Int. J.*, **27**(5), 555-566.
- Ng, T. and Lam, K. (1999), "Dynamic stability analysis of cross-ply laminated cylindrical shells using different thin shell theories", *Acta Mechanica*, **134**(3-4), 147-167.
- Ovesy, H. and Fazilati, J. (2014), "Parametric instability analysis of laminated composite curved shells subjected to non-uniform in-plane load", *Compos. Struct.*, **108**, 449-455.
- Panda, H., Sahu, S. and Parhi, P. (2015), "Hygrothermal response on parametric instability of delaminated bidirectional composite flat panels", *Eur. J. Mech.-A/Solids*, **53**, 268-281.
- Pour, H.R., Arani, A.G. and Sheikhzadeh, G. (2017), "Pulsating fluid induced dynamic stability of embedded viscoelastic piezoelectric separators using different cylindrical shell theories", *Steel Compos. Struct., Int. J.*, **24**(4), 499-512.
- Pradyumna, S. and Bandyopadhyay, J. (2011), "Dynamic instability behavior of laminated hypar and conoid shells using a higher-order shear deformation theory", *Thin-Wall. Struct.*, **49**(1), 77-84.
- Qinkai, H. and Fulei, C. (2013), "Parametric instability of a rotating truncated conical shell subjected to periodic axial loads", *Mech. Res. Commun.*, **53**, 63-74.
- Reddy, J.N. (2004), *Mechanics of Laminated Composite Plates and Shells: Theory and Analysis*, CRC press.
- Reddy, J. and Liu, C. (1985), "A higher-order shear deformation theory of laminated elastic shells", *Int. J. Eng. Sci.*, **23**(3), 319-330.
- Shariyat, M. (2011), "An accurate double-superposition global-local theory for vibration and bending analyses of cylindrical composite and sandwich shells subjected to thermo-mechanical loads", *Proceedings of the Institution of Mechanical Engineers, Part C: Journal of Mechanical Engineering Science*, **225**(8), 1816-1832.
- Sofiyev, A.H. and Kuruoglu, N. (2018), "Determination of the excitation frequencies of laminated orthotropic non-homogeneous conical shells", *Compos. Part B: Eng.*, **132**, 151-160.
- Sofiyev, A.H., Zerin, Z., Allahverdiev, B.P., Hui, D., Turan, F. and Erdem, H. (2017), "The dynamic instability of FG orthotropic conical shells within the SDT", *Steel Compos. Struct., Int. J.*, **25**(5), 581-591.
- Tornabene, F., Fantuzzi, N., Baccocchi, M., Neves, A.M. and Ferreira, A.J. (2016), "MLSDQ based on RBFs for the free vibrations of laminated composite doubly-curved shells", *Compos. Part B: Eng.*, **99**, 30-47.
- Tornabene, F., Fantuzzi, N. and Baccocchi, M. (2017), "A new doubly-curved shell element for the free vibrations of arbitrarily shaped laminated structures based on Weak Formulation IsoGeometric Analysis", *Compos. Struct.*, **171**, 429-461.
- Wu, C.-P. and Chiu, S.-J. (2002), "Thermally induced dynamic instability of laminated composite conical shells", *Int. J. Solids Struct.*, **39**(11), 3001-3021.

CC

Appendix A

In Eqs. (2)-(5), u_{ij} and v_{ij} ($i = 1, 2, 3; j = 1, 2, \dots, 8$), and u_i ($i = 3, 4$) are expressed as

$$u_{13} = A_{11}^2, u_{14} = A_{12}^2, u_{15} = A_{15}^1, u_{18} = A_{18}^1,$$

$$u_{23} = A_{21}^2, u_{24} = A_{22}^2, u_{25} = A_{25}^1,$$

$$u_{28} = A_{28}^1, u_{32} = 2A_{66}^2, u_{35} = A_{35}^1,$$

$$u_{38} = A_{38}^1, v_{11} = \frac{A_{22}^0}{B}, v_{12} = -\frac{A_{12}^0}{B},$$

$$v_{15} = \frac{A_{25}^0 A_{12}^0 - A_{15}^0 A_{22}^0}{B}, v_{18} = \frac{A_{28}^0 A_{12}^0 - A_{18}^0 A_{22}^0}{B},$$

$$v_{21} = -\frac{A_{21}^0}{B}, v_{22} = \frac{A_{11}^0}{B}, v_{25} = \frac{A_{15}^0 A_{21}^0 - A_{25}^0 A_{11}^0}{B}, \quad (A1)$$

$$v_{31} = \frac{1}{A_{66}^0}, v_{28} = \frac{A_{18}^0 A_{21}^0 - A_{28}^0 A_{11}^0}{B},$$

$$v_{35} = \frac{A_{35}^0}{A_{66}^0}, v_{38} = \frac{A_{38}^0}{A_{66}^0}, B = A_{11}^0 A_{22}^0 - A_{12}^0 A_{21}^0,$$

$$u_3 = \sum_{k=1}^N \int_{-h/2+(k-1)h/N}^{-h/2+kh/N} f_1^{(k)}(z) dz,$$

$$u_4 = \sum_{k=1}^N \int_{-h/2+(k-1)h/N}^{-h/2+kh/N} f_2^{(k)}(z) dz.$$

where

$$A_{11}^{k_1} = \sum_{k=1}^N \frac{E_{11}^{(k)}}{1 - \nu_{12}^{(k)} \nu_{21}^{(k)}} \mathfrak{R}_1, \quad A_{12}^{k_1} = \sum_{k=1}^N \frac{\nu_{21}^{(k)} E_{11}^{(k)}}{1 - \nu_{12}^{(k)} \nu_{21}^{(k)}} \mathfrak{R}_1,$$

$$A_{21}^{k_1} = \sum_{k=1}^N \frac{\nu_{12}^{(k)} E_{22}^{(k)}}{1 - \nu_{12}^{(k)} \nu_{21}^{(k)}} \mathfrak{R}_1, \quad A_{22}^{k_1} = \sum_{k=1}^N \frac{E_{22}^{(k)}}{1 - \nu_{12}^{(k)} \nu_{21}^{(k)}} \mathfrak{R}_1,$$

$$A_{66}^{k_1} = \sum_{k=1}^N G_{12}^{(k)} \mathfrak{R}_1, \quad A_{15}^{k_2} = \sum_{k=1}^N \frac{E_{11}^{(k)}}{1 - \nu_{12}^{(k)} \nu_{21}^{(k)}} \mathfrak{R}_2,$$

$$A_{18}^{k_2} = \sum_{k=1}^N \frac{\nu_{21}^{(k)} E_{11}^{(k)}}{1 - \nu_{12}^{(k)} \nu_{21}^{(k)}} \mathfrak{R}_3, \quad A_{25}^{k_2} = \sum_{k=1}^N \frac{\nu_{12}^{(k)} E_{22}^{(k)}}{1 - \nu_{12}^{(k)} \nu_{21}^{(k)}} \mathfrak{R}_2,$$

$$A_{28}^{k_2} = \sum_{k=1}^N \frac{E_{22}^{(k)}}{1 - \nu_{12}^{(k)} \nu_{21}^{(k)}} \mathfrak{R}_3, \quad A_{35}^{k_2} = \sum_{k=1}^N G_{12}^{(k)} \mathfrak{R}_2, \quad (A2)$$

$$A_{38}^{k_2} = \sum_{k=1}^N G_{12}^{(k)} \mathfrak{R}_3,$$

$$\mathfrak{R}_1 = \int_{-h/2+(k-1)h/N}^{-h/2+kh/N} z^{k_1} dz, \quad k_1 = 0, 1, 2,$$

$$\mathfrak{R}_2 = \int_{-h/2+(k-1)h/N}^{-h/2+kh/N} z^{k_2} u_1^{(k)}(z) dz,$$

$$\mathfrak{R}_3 = \int_{-h/2+(k-1)h/N}^{-h/2+kh/N} z^{k_2} u_2^{(k)}(z) dz, \quad k_2 = 0, 1.$$

in which

$$u_1^{(k)}(z) = \frac{1}{G_{13}^{(k)}} \int_0^z \frac{df_1^{(k)}(z)}{dz} dz,$$

$$u_2^{(k)}(z) = \frac{1}{G_{23}^{(k)}} \int_0^z \frac{df_2^{(k)}(z)}{dz} dz$$

(A3)

Appendix B

η_{ij} ($i, j = 1, 2, 3, 4$), λ_ρ and λ_{ax} are given as

$$\begin{aligned} \eta_{12} = & -\frac{0.25[1-r_0^{2(1-b)}]\bar{m}^2}{r_2^4[(b-1)^2+\bar{m}^2](b-1)}\left\{-u_{13}[(3b-4)b^3+2b(b+2)\bar{m}^2-\bar{m}^4]\right. \\ & + (u_{14}+u_{32})\bar{n}^2[b(b-2)+\bar{m}^2]+(4u_{14}+4u_{32}+u_{24})\bar{n}^2+(u_{23}+5u_{13}-u_{14}) \\ & \times (2b^3+(2b+1)\bar{m}^2-3b^2)+(4u_{14}-4u_{23}-7u_{13}+u_{24})[b(b-2)+\bar{n}^2] \\ & \left.-3(u_{14}+u_{24}+u_{32})\bar{n}^2-3(u_{23}+u_{13}-u_{14}-u_{24})\right\} \\ \eta_{13} = & \frac{(1-r_0^{1-2b})\bar{m}}{(2b-1)[(2b-1)^2+4\bar{m}^2]r_2^3}\left\{u_{35}[(2b-1)b+2\bar{m}^2]\bar{n}^2\right. \\ & -u_{15}[(2b-1)\lambda^3+3b\bar{m}^2-2\bar{m}^4]+2u_{15}+u_{25})(\bar{m}^2-b^2+2b^3+2b\bar{m}^2)-2u_{25}[(2b-1)b+2\bar{m}^2]\Big\} \\ & -\frac{(1-r_0^{1-2b})\bar{m}}{(2b+1)[(2b+1)^2+4\bar{m}^2]r_2^3}\left\{-u_3[b(1+2b)+2\bar{m}^2]r_2^2+u_{35}(2b+1)\bar{n}^2\right\} \\ \eta_{14} = & \frac{(1-r_0^{1-2b})\bar{n}}{r_2^3[(2b-1)^2+4\bar{m}^2](2b-1)}\left\{-2(u_{38}+u_{18})\bar{m}^2[(b-1)b+\bar{m}^2]-(2u_{18}+2u_{38}-3u_{28})\bar{m}^2\right\} \\ \eta_{22} = & -\frac{(1-r_0^{1-2b})\bar{m}^2\bar{n}^2}{[(2b-1)^2+4\bar{m}^2](2b-1)r_2^3}\left\{-2(u_{32}+u_{23})[(b-1)b+\bar{m}^2]-2u_{24}\bar{n}^2-u_{32}-u_{23}+u_{24}\right\} \\ \eta_{23} = & \bar{m}\bar{n}^2\left\{\frac{(u_{25}+u_{35})[(2b-1)b+2\bar{m}^2](1-r_0^{1-2b})}{[(2b-1)^2+4\bar{m}^2](2b-1)r_2^3}+\frac{u_{35}(1-r_0^{-2b})}{4(\bar{m}^2+b^2)r_2^2}\right\} \\ \eta_{24} = & -\frac{\bar{m}^2\bar{n}}{4}\left\{\frac{[u_{38}(\bar{m}^2+b^2)+u_{28}\bar{n}^2](1-r_0^{-2b})}{br_2^2(\bar{m}^2+b^2)}+\frac{u_4[1-r_0^{-2(b+1)}]}{(b+1)[(b+1)^2+\bar{m}^2]}\right\} \\ \eta_{31} = & \frac{1}{4}\frac{\bar{m}^2(1-r_0^{-2b})}{b(\bar{m}^2+b^2)r_2^3}\left\{v_{11}\bar{n}^4+(v_{31}+v_{21}+v_{12})\bar{n}^2(b^2-1+\bar{m}^2)+(2v_{31}+3v_{21}+v_{12})\bar{n}^2\right. \\ & - (v_{31}+2v_{21}+2v_{11})\bar{n}^2+v_{22}[\bar{m}^4-(b+1)^3(3b-1)-2(b+3)(b+1)\bar{m}^2] \\ & + (4v_{22}+v_{12}-v_{21})(2\bar{m}^2b-1+3b^2+3\bar{m}^2+2b^3) \\ & \left.- (5v_{22}+3v_{12}-3v_{21}-v_{11})(\bar{m}^2+b^2-1)+2(v_{11}+v_{21}-v_{22}-v_{12})\right\} \\ \eta_{33} = & \frac{\bar{m}(1-r_0^{-2b})}{4r_2^3b}\left\{[v_{35}+v_{15})\bar{n}^2-v_{25}(b^2-\bar{m}^2)-(v_{25}+v_{15})b-v_{15}]\right. \\ \eta_{34} = & \frac{(1-r_0^{-2b})\bar{m}^2}{4b(\bar{m}^2+b^2)r_2^3}\left[v_{18}\bar{n}-v_{18}\bar{n}^3-(v_{38}+v_{28})\bar{n}(\bar{m}^2+b^2)\right] \end{aligned}$$

$$\begin{aligned}
\eta_{32} &= \frac{(1 - r_0^{-2b}) \bar{m}^2}{4br_2^3 \tan \alpha} \\
\eta_{41} &= -\frac{\bar{m}^2 (1 - r_0^{-2b})}{4r_2^2 b \tan \alpha}, \quad \eta_{43} = -\frac{\bar{m} [1 - r_0^{-(1+2b)}] [2\bar{m}^2 + 2b^2 + 3b + 1] \mu_3}{r_2 [(2b+1)^2 + 4\bar{m}^2] (2b+1)} \\
\eta_{44} &= \frac{2u_4 [1 - r_0^{-(1+2b)}] \bar{m}^2 \bar{n}}{r_2 (2b+1) [2(b+1)^2 + 4\bar{m}^2]} \\
\lambda_\rho &= \frac{[1 - r_0^{-2(1+b)}] \bar{m}^2}{4[(b+1)^2 + \bar{m}^2] (b+1)}, \quad \lambda_{ax} = \frac{[1 - r_0^{-2b}] \bar{m}^2}{4r_2^2 b}
\end{aligned} \tag{B1}$$